Research article

Fei Zhang, Qingyu Zeng, Mingbo Pu, Yanqin Wang, Yinghui Guo, Xiong Li, Xiaoliang Ma and Xiangang Luo*

Broadband and high-efficiency accelerating beam generation by dielectric catenary metasurfaces

https://doi.org/10.1515/nanoph-2020-0057
Received January 27, 2020; accepted April 22, 2020

Abstract: Self-accelerating beams show considerable captivating phenomena and applications owing to their transverse acceleration, diffraction-free and self-healing properties in free space. Metasurfaces consisting of dielectric or metallic subwavelength structures attract enormous attention to acquire self-accelerating beams, owing to their extraordinary capabilities in the arbitrary control of electromagnetic waves. However, because the self-accelerating beam generator possesses a large phase gradient, traditional discrete metasurfaces suffer from insufficient phase sampling, leading to a low efficiency and narrow spectral band. To overcome this limitation, a versatile platform of catenary-inspired dielectric metasurfaces is proposed to endow arbitrary continuous wavefronts. A high diffraction efficiency approaching 100% is obtained in a wide spectral range from 9 to 13 μm. As a proof-of-concept demonstration, the broadband, high-efficiency and high-quality self-accelerating beam generation is experimentally verified in the infrared band. Furthermore, the chiral response of the proposed metasurfaces enables the spin-controlled beam acceleration. Considering these superior performances, this design methodology may find wide applications in particle manipulation, high-resolution imaging, optical vortex generation, and so forth.

Keywords: catenary metasurfaces; pancharatnam-berry phase; self-accelerating beams; subwavelength structures.

1 Introduction

In recent decades, diffraction-free waves have attracted enormous attentions [1, 2]. As a sort of special dispersion-free beams, Airy beams [3] or, more generally, self-accelerating beams [4, 5] bear not only self-healing properties but also possess a unique transverse acceleration characteristic since their main peaks propagate along a nonlinear curve. Self-accelerating beams have considerable applications in various fields, such as filamentation [6], imaging [7], light bullet [8], and optical manipulation [9]. Recently, there have been abundant investigations on the generation of self-accelerating beams [10, 11]. Traditional methods usually acquire self-accelerating beams in the Fourier domain by encoding a cubic-phase distribution in liquid crystal spatial light modulators [12, 13] or adaptive deformable mirrors [14]. The applications of self-accelerating beams in the compact nanophotonic platform are mainly hindered by both those hulking elements and the extraordinary long working distance of the Fourier Transform system.

To date, various methods have been proposed to avoid defects in traditional methods. Metasurface [15, 16], which is composed of subwavelength structures, is one of the prospective choices due to its ability to achieve arbitrary wavefront manipulation at the subwavelength scale. Over the past decades, many exotic phenomena and extraordinary flat optical devices have been realized, such as

Fei Zhang and Qingyu Zeng: These authors contributed equally to this work.

***Corresponding author: Xiangang Luo**, State Key Laboratory of Optical Technologies on Nano-Fabrication and Micro-Engineering, Institute of Optics and Electronics, Chinese Academy of Sciences, Chengdu, 610209, China; and School of Optoelectronics, University of Chinese Academy of Sciences, Beijing, 100049, China, E-mail: lxg@ioe.ac.cn. https://orcid.org/0000-0002-1401-1670
Fei Zhang: State Key Laboratory of Optical Technologies on Nano-Fabrication and Micro-Engineering, Institute of Optics and Electronics, Chinese Academy of Sciences, Chengdu, 610209, China; Key Laboratory of Optoelectronic Technology and System, Ministry of Education, Chongqing University, Chongqing, 400030, China
Qingyu Zeng: State Key Laboratory of Optical Technologies on Nano-Fabrication and Micro-Engineering, Institute of Optics and Electronics, Chinese Academy of Sciences, Chengdu, 610209, China
Mingbo Pu, Yanqin Wang, Yinghui Guo, Xiong Li and Xiaoliang Ma: State Key Laboratory of Optical Technologies on Nano-Fabrication and Micro-Engineering, Institute of Optics and Electronics, Chinese Academy of Sciences, Chengdu, 610209, China; School of Optoelectronics, University of Chinese Academy of Sciences, Beijing, 100049, China

broadband spin Hall effect [17, 18], asymmetric photonic spin–orbit interactions [19–21], invisibility cloaks [22, 23], full-color 3D holography [24, 25], nanoprint-hologram display [26, 27], achromatic metalens [28, 29], among many others [30, 31]. At the same time, metasurfaces have also been applied to generate self-accelerating beams in the spatial domain [32–34], and Airy surface plasmons have also been demonstrated via on-chip nanostructures [35–37]. However, such self-accelerating beam generators need to be encoded with a cubic phase profile whose phase gradient is so large that contemporary discrete metasurfaces still face the problem of insufficient phase sampling in the edge region, resulting in strong spurious diffraction orders which will destroy the accelerating beam trajectory. As an alternative way, one can increase the sampling by reducing the period of discrete structures. Unfortunately, the smallest period will be limited by the fabrication feasibility and electromagnetic coupling between adjacent elements [38, 39]. To balance these two factors, existing discrete metasurfaces still possess a limited efficiency and spectral band [33, 34]. Continuous components like metallic catenary-structures and dielectric nanoarc-structures have exhibited prospects to remove the shortcomings of discrete metasurfaces [40–43], but they still suffer from low efficiency or obvious spurious diffraction orders [44].

In this paper, a methodology for dielectric catenary (a form of integral) metasurfaces is proposed to detour the aforementioned limitations. Excellent performances of the integral structure are attributable to the ability of continuous wavefront manipulating within a single element. It provides a significant way to alleviate insufficient sampling of metasurfaces with large phase gradients under the premise of ensuring the efficiency and bandwidth of the device. A broadband and high-efficiency self-accelerating beam generator with a cubic phase profile has been realized by the proposed integral metasurface. Owing to the chiral response of the proposed generator, mirrored accelerating trajectories can be acquired via altering the spin state of the incident light. This work may provide a new designing strategy for other metadevices, including high-resolution metalens, optical orbital angular momentum generators, and optical tweezers.

2 Results and discussion

2.1 Structure design

Unlike Airy beams with a defined quadratic trajectory, self-accelerating beams with customized beam trajectories can be designed based on the geometrical optical framework. To derive the phase distribution of the metasurface that produces the self-accelerating beam, as shown in Figure 1A, we assume that the metasurface is located on $z = 0$ plane and the accelerating beam follows the trajectory of $z = f(x)$. (x_0, z_0) is the coordinate of an arbitrary point on the trajectory curve and its tangential equation is $z = f'(x_0)\cdot(x - x_0) + z_0$. Then one can get the intersection of the tangent and metasurface, that is, $x = x_0 - z_0/f'(x_0)$. According to the principle of geometric optics, the phase gradient $d\varphi(x)/dx$ imparted by the metasurface has to be amenable to the equation: $d\varphi(x)/dx = -k_0/f'(x_0)$, where $k_0 = 2\pi/\lambda$ is the wavenumber and λ is the wavelength in free space. Finally, the phase distribution $\varphi(x)$ can be described as:

$$\varphi(x) = \int \frac{-k_0}{f'(x_0)} dx \tag{1}$$

According to Eq. (1), the trajectory of the two-dimensional reciprocal self-accelerating beam is $\begin{cases} z = a/x \\ z = a/y \end{cases}$, where a is a constant, and the phase distribution $\varphi(x)$ can be defined by:

$$\varphi(x, y) = k_0 (x^3 + y^3)/12a \tag{2}$$

The reciprocal curve and phase distribution of the generator are shown in Figure 1B. Once the phase distribution is determined, the generator can be engineered with different subwavelength structures. According to Eq. (2), the phase gradient of the cubic phase is $d\varphi(x)/dx = k_0 x^2/6a$, which

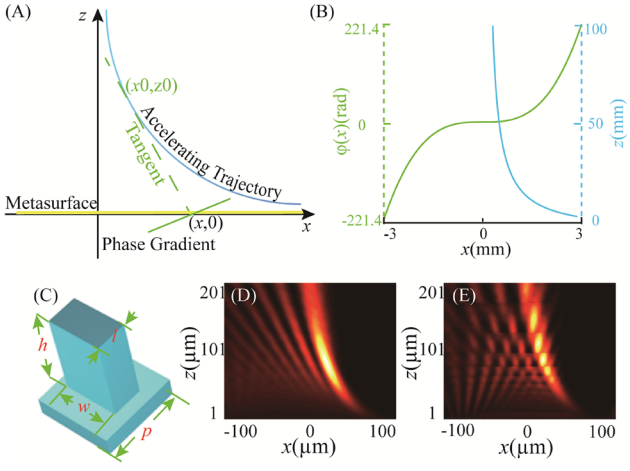

Figure 1: (A) Schematic diagram of deducing phase distribution for generating the self-accelerating beam trajectory based on geometrical optical framework. (B) Reciprocal self-acceleration trajectory (blue) and the phase distribution (green) of the generator. (C) Schematic illustration of the rectangular antenna. (D, E) Simulated trajectories of the discrete metasurfaces whose lattice constants are 0.1λ and 0.7λ, respectively.

would be too large to sufficiently sample the phase using traditional discrete metasurfaces. For example, the phase gradient will be k_0 at $x = \sqrt{6a}$, and thus there are usually two or fewer structures to sample the wavefront manipulation within a single period covering $0 \sim 2\pi$, leading to a low efficiency and narrow bandwidth. To discuss this issue in detail, we theoretically simulated a 200 × 200 μm self-accelerating generator with a phase gradient of k_0 at its edge (i. e., the radius of the generator is equal to $\sqrt{6a}$) by vectorial angular spectrum theory [40]. It is assumed that this device consists of discrete rectangular antennas shown in Figure 1C, thus the phase will be sampled with a period of p in the simulation. The details of the simulation are illustrated in Section 1 of Supplementary Information. Figure 1D and E presents the simulated results for the sampling periods of 0.1λ and 0.7λ, respectively, and the results for other sampling periods are shown in Figure S1. The layered main lobes indicate that the trajectory of the main peak will no longer follow the presupposed curve as the period increases (Figure 1E), which is mainly caused by spurious diffraction orders from the area at the edge due to the insufficient phase sampling. Simulated results indicate that discrete structures with smaller lattice constants should be used to obtain high-quality acceleration trajectories and near stable results can be acquired when the lattice constant is less than 0.4λ. On the other hand, two issues of harder fabrication and worse performance will emerge when the period becomes smaller. The performances of efficiency and bandwidth of the discrete structures are shown in Figure S2. In a word, traditional discrete metasurfaces rarely ensure high efficiency, wide spectral band, and sufficient sampling simultaneously. Thus, it is essential to design subwavelength blocks with the continuous wavefront manipulation ability for the metadevices with a large phase gradient, such as self-accelerating beam generators.

Owing to its continuous wavefront manipulation ability, the proposed integral dielectric structure provides an opportunity to eliminate this contradiction between the large phase gradient and the performance of the generator. The simulation results of the integral and discrete structures are used to highlight the advantages of integral metasurfaces for achieving large phase gradients. Compared with the discrete structure, the integral structure can achieve a higher efficiency and more accurate phase distribution under the same phase gradient. The detailed explanations are shown in Supporting Information Section 1 and Figure S3. Additionally, the broadband response of the integral structure profits from the achromatic property of the Pancharatnam–Berry (PB) phase, which is determined by the orientation of the anisotropic structure and the spin state of the incident light, regardless of the wavelength. To clearly describe the broadband characteristics of the PB phase, we assume an anisotropic transmissive scatterer with an orientation angle of α, and the transmissive complex amplitudes along its fast and slow axes are t_u and t_v, respectively. When a circularly polarized (CP) light of $[1 - i\sigma]^T$ is normally incident on the anisotropic scatterer, the emergent beam can be expressed as [15]:

$$(t_u + t_v)\begin{bmatrix} 1 \\ -i\sigma \end{bmatrix} + (t_u + t_v)2^{-i\sigma\alpha}\begin{bmatrix} 1 \\ i\sigma \end{bmatrix} \quad (3)$$

where $\sigma = \pm 1$ are for right- and left-handed circular polarization (RCP and LCP), respectively. From the second term

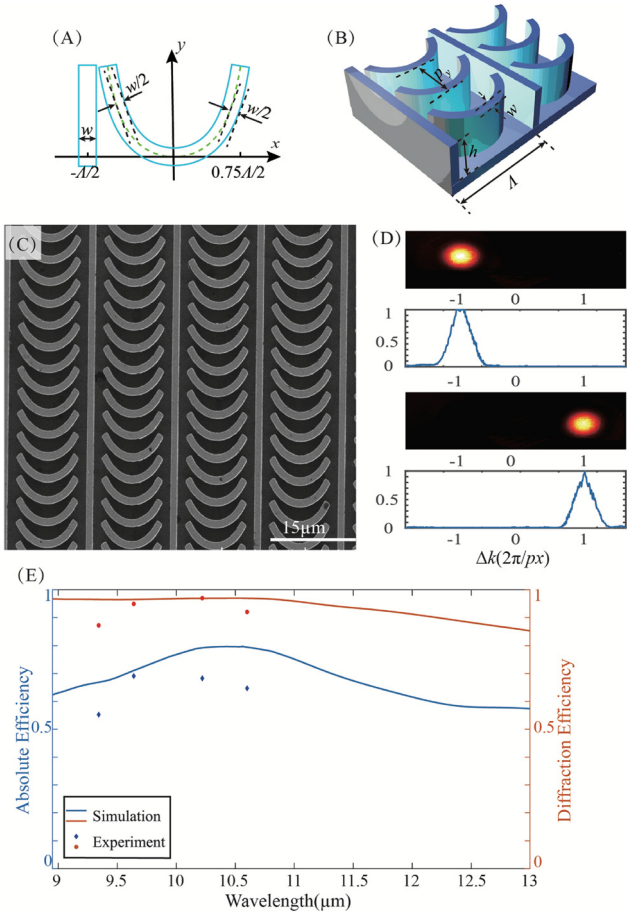

Figure 2: (A, B) 2D and 3D schematic views of the integral structure with an equal width. The geometric parameters are as follows: $w = 1.3$ μm and $h = 4.7$ μm. (C) Scanning electron microscopy (SEM) image of the deflector sample. The lattice spacings of the array are $\Lambda = 14.99$ μm and $p_y = 3.2$ μm. (D) Experimental measurement results under LCP (top) and RCP (bottom) illumination at the wavelength of 10.6 μm. (E) Simulated and measured results of absolute and diffraction efficiencies over a broad spectrum from 9 to 13 μm.

of Eq. (3), the emergent cross-polarized light will carry a PB phase of -2$\sigma\alpha$ that is independent of wavelength. One-dimensional devices are used as an example to describe the modeling process of the proposed integral dielectric metasurfaces, and the two-dimensional counterpart is shown in Section 2 of Supplementary Information. The schematic diagrams of the integral metasurface are shown in insets of Figure 2A and B. It is hypothesized that the phase $\varphi(x)$ varies from $2m\pi$ to $2(m+1)\pi$ as x moves from $a = \varphi^{-1}(2m\pi)$ to $b = \varphi^{-1}[2(m+1)\pi]$, where m is a non-negative integer and $\varphi^{-1}(x)$ represents the inverse function of $\varphi(x)$. Then, the slope of the continuous structure should be $y' = \tan[\varphi(x)/2]$ according to the PB phase principle, and the structural streamline can be derived by the mathematical integration along the x-axis:

$$y = \int_a^b \tan(\varphi(x)/2)dx \tag{4}$$

Then, two curves, which are located on the separated edges of the streamline with the same distance of $w/2$ along the normal of the streamline, are closed to build the proposed integral structure. Compared with the previous method for constructing the metallic one by two streamlines with a longitudinal shift [43], the proposed method can enable not only higher efficiency but also higher fabrication feasibility (see Figure S5). To avoid intersection or tiny spacing (limited by the fabrication resolution) between adjacent structures, the integration interval will be truncated at $x = a + 0.125\Lambda$ and $x = b - 0.125\Lambda$, where $\Lambda = b - a$. Subsequently, vertical structures with the same width are employed in the truncated region to acquire continuous phase retardation and consistent amplitude response, and the number of vertical structures is $\lfloor 0.125\Lambda/w \rfloor$, where $\lfloor y \rfloor$ represents the round down function of y.

2.2 Experiments and discussions

As a proof-of-concept demonstration, a spin-dependent deflector consisting of the same integral dielectric structure has been designed, fabricated, and chdaracterized. In synergy with the spin-Hall effect of light originating from the photonic spin–orbit interactions, the periodic array of the linear integral structures with a constant phase gradient can provide the same function as the deflector. The lattice constants of the array in the x- and y- directions are, respectively, set to 14.99 μm and 3.2 μm (the diffraction angle of -1st order is −45° in the x-direction at 10.6 μm wavelength), and the height and width of integral structures are 4.7 μm and 1.3 μm, respectively. Then, a 5 × 5 mm sample has been fabricated to experimentally verify the methodology, and the partial scanning electron microscopy images of the sample are shown in Figure 2C. Since the employed laser has a limited bandwidth from 9.32 μm to 10.69 μm, the laser lights at different wavelengths with strong and stable power have been selected for experiments to reduce the effects of background thermal noise on experiment results. Furthermore, the broadband and high-efficiency characteristics can be proved by these four discrete points over the band owing to the continuous efficiency spectrum of the integral structure. As shown in Figure 2E, the deflector achieves high absolute and diffractive efficiencies within a wide spectral band from 9 to 13 μm. The absolute or diffractive efficiency is defined as the ratio of the -1st diffraction energy to the incident or transmitted power. As a result, the absolute efficiency equals the total transmission multiplied by the diffraction efficiency. Experimentally, the sample has achieved high absolute and diffraction efficiencies (67.13% and 92.04%) close to simulation ones (79.4% and 96.94%) at the designed wavelength, and the measured results at other wavelengths are depicted in Figure 2E. The fact that the measured absolute efficiencies are lower than the simulated ones can be mainly attributed to material loss and fabrication error. Additionally, the high diffraction efficiency can be further validated by the measured diffraction patterns which solely contain -1st or +1st diffraction order under LCP or RCP illumination (Figure 2D), and the measured results at other wavelengths are depicted in Figure S6. Ultra-high diffraction efficiency promises to generate outstanding accelerating beams without the need for a quarter waveplate and linear polarizer to filter out the co-polarized light, which will facilitate the integration of self-accelerating beam generators into ultra-compact optical systems. Since it is hard to measure the diffraction efficiency of the self-accelerating beam accurately, especially in the invisible infrared band, the efficiency performance of the deflector is used to indirectly represent that of the self-accelerating beam generator.

Owing to these superior performances, the proposed method can be applied to implement a self-accelerating beam generator. Due to the limitation of the mechanical structure of the employed infrared detector, it is only possible to directly measure the diffraction pattern located at a distance of more than 3 mm from the generator. Therefore, we have designed an integral dielectric metasurface (6 × 6 mm) that can generate a reciprocal self-accelerating beam far enough to facilitate detection, and the acceleration coefficient a of the reciprocal curve ($z = a/x$) is set to $12000D$, where $D = 6$ mm is the diameter of the generator. Partial scanning electron microscopy

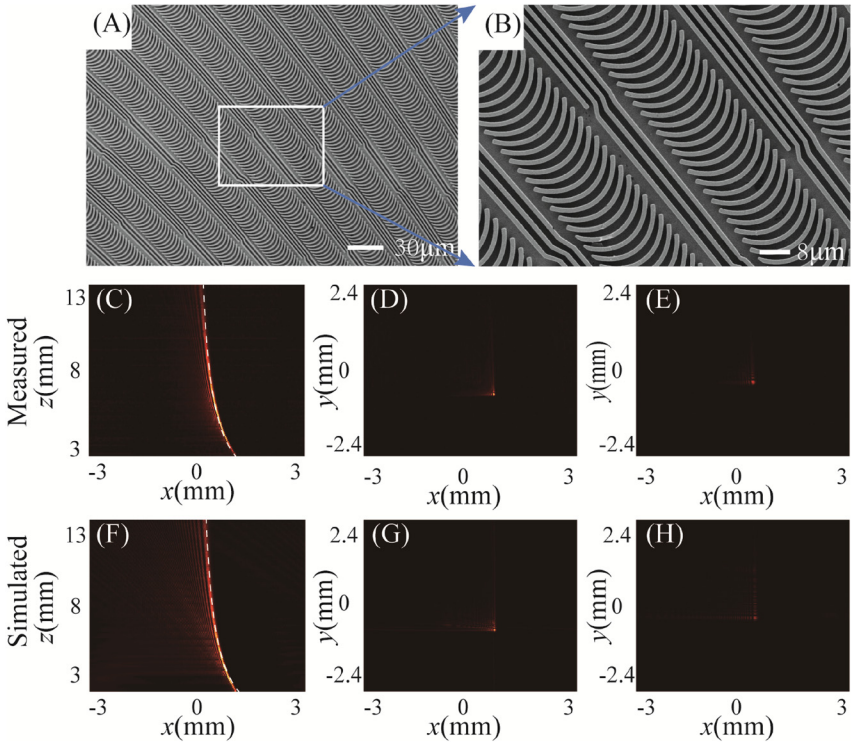

Figure 3: (A, B) SEM images of the self-accelerating beam generator. (C, F) Measured and simulated self-accelerating beam trajectories on the *x-z* plane. The white dotted lines are theoretical trajectories. (D, G) Measured and simulated diffraction patterns on the *x-y* plane at $z = 5$ mm. (E, H) The measured and simulated diffraction patterns on the *x-y* plane $z = 9$ mm.

images of the generator are shown in Figure 3A and B. An electronically controlled movement platform (GCD-0401 M) with the accuracy of 1 μm is placed along the optical axis to measure the intensity distribution at different distances from the generator, and the schematic illustration of the experimental setup is shown in Figure S7. The measured self-accelerating trajectory at the wavelength of 10.6 μm along the optical axis is represented in Figure 3C, and Figure 3F shows the simulated result for comparison. From the measured and simulated trajectories, there are little deviations between them and both trajectories accurately follow the preset reciprocal curve, which indicates that the contradiction between the performance and phase sampling of the generator can be solved through the proposed integral metasurfaces. Figure S8 depicts the measured full width at half maximum (FWHM) values of the beam trajectory from $z = 3$ mm to $z = 13$ mm. The fluctuant FWHM values are mainly attributable to the large pixel size of the detector (8.5 μm) and background thermal noise. As a result, the fitting curve of experimental data is used to characterize the difference between experimental and simulated results. In this case, the excellent performance of the integral generator has been demonstrated by the fact that the fitting curve of experimental data agrees well with

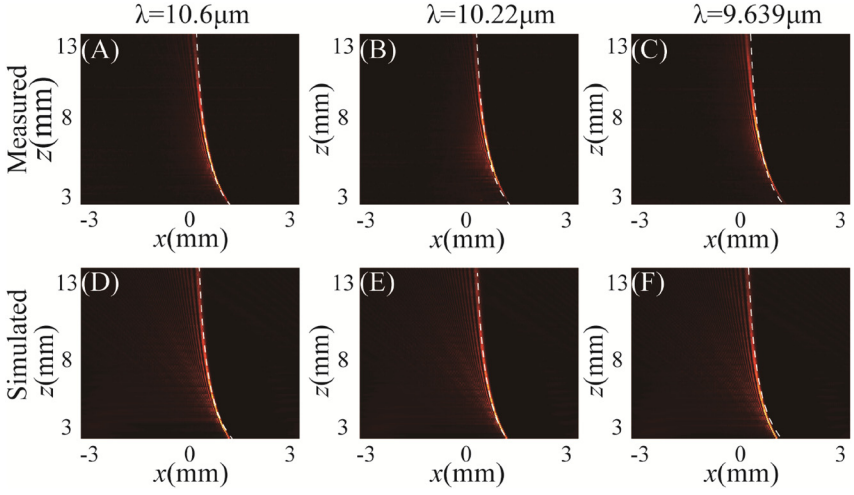

Figure 4: (A–C) Measured and (D–F) simulated self-accelerating trajectories on the *x-z* plane at three wavelengths under LCP incidence.

the simulated one. Additionally, it can be seen that the main lobe of the beam maintains a spot size about 48 μm within a long propagation distance from z = 4 mm to z = 6 mm (~200λ, see Figure S8), which is an explicit validation for the non-diffraction characteristic of self-accelerating beams. To further demonstrate the performance of the self-accelerating beam, the measured intensity distributions at z = 5 mm and z = 9 mm are shown in Figure 3D and E, respective, and both them show a good agreement with their corresponding theoretical counterparts (Figure 3G and H). Deviations between experimental and theoretical results could be attributed to fabrication and experimental errors.

Stable self-acceleration trajectories should also be obtained under the illuminating beams at different wavelengths benefiting from the achromatic characteristic of the PB phase, and the accelerating trajectories at three wavelengths of 9.639, 10.22 and 10.6 μm have been measured to verify it. Those measured results are depicted in Figure 4A–C, and the corresponding theoretical results are shown in Figure 4D–F for comparisons. These results show that excellent self-acceleration trajectories can also be acquired over a wide spectral range, and we have measured FWHM values similar to the simulated ones along the three acceleration trajectories (Figure S8). The defect of narrow

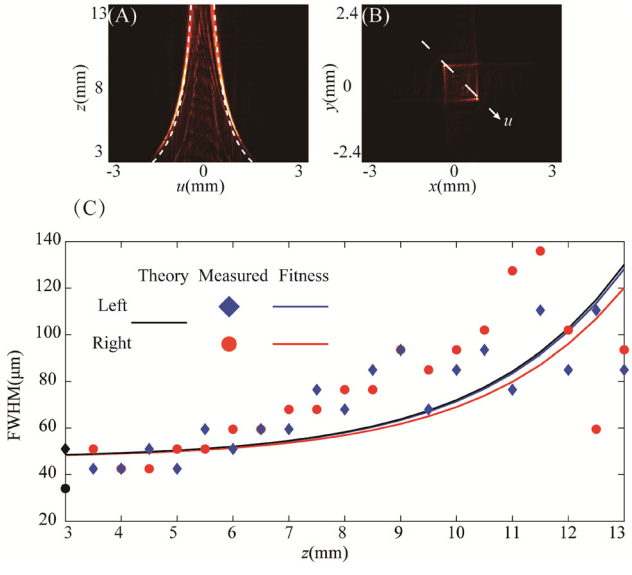

Figure 5: Measured results under linearly polarized incidence. (A) The measured self-accelerating trajectories on the u-z plane, where u is the line between the two symmetric major lobes. The white dotted lines are theoretical trajectories. (B) Measured diffraction pattern on the x-y plane at z = 7 mm. (C) The measured FWHM values of left and right ones at the wavelength of 10.6 μm, and the blue and red curves are the fitted curve of the measured data. The black curve is the theoretical curve.

band caused by the discrete strategy can be solved owing to the continuity of the phase regulation of the integral metasurface. The position of the main lobe will shift as the wavelength changes, which means that the self-accelerating trajectory is dispersive. This phenomenon primarily derives from the theoretical inherent evolution. According to the above theoretical analyses, the coefficient of the self-acceleration trajectory is $a \propto 1/k$, which means that the beam trajectory is related to not only the phase distribution but also the wave vector of the incident light. As a result, the beam trajectory changes with the incident wavelength even under the same phase distribution, and it will gradually move toward the origin of the coordinate as the wavelength decreases. This standpoint can also be verified by the simulation results that have similar deviations. Furthermore, the fact that the integral metasurface achieves a consistent PB phase distribution over broadband can be proved by the beam trajectory that correctly evolves with the incident wave vector, as shown in Figure 4.

According to the principle of the PB phase, the transmitted cross-polarized light will carry an opposite phase gradient for two opposite spin states, resulting in the spin-dependent response of the integral metasurface. This implies that the self-accelerating trajectory with axial symmetry along the z-axis will be obtained when the generator is illuminated by CP light with an opposite spin state. Since linearly polarized light can be seen as a superposition of RCP and LCP, two mirrored self-accelerating trajectories will be acquired when the metasurface is illuminated by the linearly polarized light. The measured trajectory at 10.6 μm wavelength is shown in Figure 5A, and Figure 5B presents the intensity pattern at z = 7 mm. Figure S9 shows the simulated result for comparisons. As expected, two symmetrical self-accelerating trajectories have been observed in experiments and match well with the theoretical predictions. Furthermore, Figure 5C depicts the FWHM values of two mirrored trajectories, and the slight difference between the left and right beam trajectories can be attributed to non-absolute normal illumination during the experiments. Furthermore, the FWHM values from z = 10 mm to z = 13 mm are somewhat unstable because the light intensity of the beam trajectory gradually weakens along the propagation and thus the effect of environmental noise is gradually significant. In a word, the beam trajectory can be controlled by the polarization state of the incident light within acceptable error. Adjustable beam trajectories provide the possibility of microscopic particle manipulation with adjustable trajectories. Besides, rotary trajectories can be obtained by adjusting the incident angle (Figure S10, Supporting Information).

3 Conclusion

In conclusion, an effective methodology has been proposed to design catenary-type metasurfaces with the ability of continuous wavefront manipulation. The proposed platform not only solves the problem of insufficient phase sampling for discrete metasurfaces, but also enables high-efficiency and broadband wavefront manipulation. Profiting from near-perfect phase manipulation of the proposed integral structure, a spin-dependent deflector with nearing 100% diffraction efficiency over a wide spectral range has been demonstrated. Furthermore, as a representative of meta-devices with a large phase gradient, a self-accelerating beam generator has been implemented to directly excite the reciprocal accelerating beam in the spatial domain. Additionally, incorporating with the chiral response of the proposed integral metasurface, two mirrored trajectories have been experimentally proved under the illumination of two orthogonal CP lights. This work provides a promising way to design more spin-dependent multifunctional meta-devices beyond deflectors and accelerating beam generators, and may find wide applications in high-resolution imaging and particle manipulation.

4 Methods

4.1 Simulations

The optical properties of the integral dielectric structure were simulated by the finite element method in CST Microwave Studio. The boundary conditions in the *x*-, *y*-, and *z*-directions are unit-cell, unit-cell, and open, respectively. Enough diffraction orders have been calculated. The permittivity of silicon was set to 11.36 in the simulations [19]. All electric-field simulations of self-accelerating beam generators are based on vectorial angular spectrum theory [40]. During the simulation, the cubic phase matrix of size $[l/p] \times [l/p]$ is generated with a sample period of p, and then is interpolated to a matrix of $[l/0.1\lambda] \times [l/0.1\lambda]$ by the nearest neighbor interpolation, where $[\xi]$ represents the round function of ξ; l is the size of the generator. For discrete metasurfaces, p depends on the period of unit elements. Since the catenary metasurface can support a continuous wavefront, p should be small enough and is equal to 0.1λ in our simulations.

4.2 Sample fabrication

First, a 500 nm thick AZ 1500 photoresist layer was spin-coated onto a double-sided polished Si wafer (wafer thickness is ~500 μm) and baked at 100 °C for 5 min. Then, the patterns of metasurfaces were fabricated through the direct laser writing in the photoresist at 22 °C and 50% humidity. Next, the photoresist patterns were obtained by developing in the AZ 400 K for 50 s. After development, the sample was baked at 100 °C for 10 min. Subsequently, the photoresist patterns are transferred into Si wafer to form the structures via the inductive-coupled plasmonic etching under the SF_6 gas condition, combined with Bosch process under the C_4F_8 gas condition. After etching to the set thickness, the residual photoresist was removed under the O_2 gas condition.

4.3 Characterizations

As shown in Figure S7, a tunable CO_2 laser was employed as the light source in the experiment. The beam successively passed through the adjustable attenuator, linear polarizer, quarter waveplate, and a scalable aperture, and then transmitted through the sample. For the efficiency characterization of the deflector, an infrared power meter was used to measure the optical power of incident and transmissive lights. The transmitted diffraction patterns were recorded by an infrared detector whose pixel size is 17×17 μm with a video capture card (TC-UB625), and the images were magnified two times through the built-in interpolation algorithm during the experiment, that is, the effective pixel size is 8.5×8.5 μm. The infrared detector, which is assembled on an electronically controlled movement platform with the accuracy of 1 μm, can be moved precisely along the optical axis.

Acknowledgments: This work was supported by the National Natural Science Foundation of China (61975210).
Competing interests: The authors declare no competing interest.

References

[1] R. Wang, Y. Wang, D. Zhang, et al., "Diffraction-free Bloch surface waves," *ACS Nano*., vol. 11, pp. 5383–5390, 2017, https://doi.org/10.1021/acsnano.7b02358.s001.
[2] H. E. Kondakci, and A. F. Abouraddy, "Diffraction-free space–time light sheets," *Nat. Photon.*, vol. 11, p. 733, 2017, https://doi.org/10.1364/isa.2017.iw4e.6.
[3] G. A. Siviloglou, J. Broky, A. Dogariu, and D. N. Christodoulides, "Observation of accelerating airy beams," *Phys. Rev. Lett.*, vol. 99, p. 213901, 2007, https://doi.org/10.1103/physrevlett.99.213901.
[4] I. Kaminer, M. Segev, and D. N. Christodoulides, "Self-accelerating self-trapped optical beams," *Phys. Rev. Lett.*, vol. 106, p. 213903, 2011, https://doi.org/10.1103/physrevlett.106.213903.
[5] R. Schley, I. Kaminer, E. Greenfield, R. Bekenstein, Y. Lumer, and M. Segev, "Loss-proof self-accelerating beams and their use in non-paraxial manipulation of particles' trajectories," *Nat. Commun.*, vol. 5, p. 5189, 2014, https://doi.org/10.1038/ncomms6189.
[6] P. Polynkin, M. Kolesik, J. V. Moloney, G. A. Siviloglou, and D. N. Christodoulides, "Curved plasma channel generation using ultraintense airy beams," *Science*, vol. 324, pp. 229–232, 2009, https://doi.org/10.1126/science.1169544.
[7] S. Jia, J. C. Vaughan, and X. Zhuang, "Isotropic three-dimensional super-resolution imaging with a self-bending point spread function," *Nat. Photon.*, vol. 8, p. 302, 2014, https://doi.org/10.1038/nphoton.2014.13.

[8] A. Chong, W. H. Renninge, D. N. Christodoulides, and F. W. Wise, "Airy–Bessel wave packets as versatile linear light bullets," *Nat. Photon.*, vol. 4, p. 103, 2010, https://doi.org/10.1038/nphoton.2009.264.

[9] J. Baumgartl, M. Mazilu, and K. Dholakia, "Optically mediated particle clearing using airy wavepackets," *Nat. Photon.*, vol. 2, p. 675, 2008, https://doi.org/10.1038/nphoton.2008.201.

[10] P. Zhang, Y. Hu, D. Cannan, et al., "Generation of linear and nonlinear nonparaxial accelerating beams," *Opt. Lett.*, vol. 37, pp. 2820–2822, 2012, https://doi.org/10.1364/ol.37.002820.

[11] N. Voloch-Bloch, Y. Lereah, Y. Lilach, A. Gover, and A. Arie, "Generation of electron airy beams," *Nature*, vol. 494, p. 331, 2013, https://doi.org/10.1038/nature11840.

[12] L. Froehly, F. Courvoisier, A.Mathis, et al., "Arbitrary accelerating micron-scale caustic beams in two and three dimensions," *Opt. Express.*, vol. 19, pp. 16455–16465, 2011, https://doi.org/10.1364/oe.19.016455.

[13] H. T. Dai, X. W. Sun, D. Luo, and Y. J. Liu, "Airy beams generated by a binary phase element made of polymer-dispersed liquid crystals," *Opt. Express.*, vol. 17, pp. 19365–19370, 2009, https://doi.org/10.1364/oe.17.019365.

[14] Y. Guo, M. Pu, X. Li, et al., "Chip-integrated geometric metasurface as a novel platform for directional coupling and polarization sorting by spin–orbit interaction," *IEEE J. Selected Top Quantum Elect.*, vol. 24, pp. 1–7, 2018, https://doi.org/10.1109/jstqe.2018.2814744.

[15] X. Luo, "Principles of electromagnetic waves in metasurfaces," *Sci. China-Phys. Mech. Astron.*, vol. 58, p. 594201, 2015, https://doi.org/10.1007/s11433-015-5688-1.

[16] N. Yu, P. Genevet, M. A. Kats, et al., "Light propagation with phase discontinuities: generalized laws of reflection and refraction," *Science*, vol. 334, pp. 333–337, 2011, https://doi.org/10.1126/science.1210713.

[17] X. Yin, Z. Ye, J. Rho, Y. Wang, and X. Zhang, "Photonic spin hall effect at metasurfaces." *Science*, vol. 339, pp. 1405–1407.2013, https://doi.org/10.1126/science.1231758.

[18] X.G. Luo, M.B. Pu, X. Li, and X.L. Ma, "Broadband spin Hall effect of light in single nanoapertures." *Light Sci. Appl.*, vol. 6, 2017, Art no. e16276, https://doi.org/10.1038/lsa.2016.276.

[19] F. Zhang, M. Pu, X. Li, et al., "All-dielectric metasurfaces for simultaneous giant circular asymmetric transmission and wavefront shaping based on asymmetric photonic spin-orbit interactions." *Adv. Funct. Mater.*, vol. 27, p. 1704295, 2017, https://doi.org/10.1002/adfm.201704295.

[20] F. Zhang, M. Pu, J. Luo, H. Yu, and X. Luo, "Symmetry breaking of photonic spin-orbit interactions in metasurfaces." *Opto.-Electron. Eng.*, vol. 44, pp. 319–325, 2017, https://doi.org/10.3969/j.issn.1003-501X.2017.03.006.

[21] R. C. Devlin, A. Ambrosio, N. A. Rubin, J. P. B. Mueller, and F. Capasso, "Arbitrary spin-to-orbital angular momentum conversion of light." *Science*, vol. 358, pp. 896–901, 2017, https://doi.org/10.1126/science.aao5392.

[22] X. Chen, Y. Luo, J. Zhang, K. Jiang, J. B. Pendry, and S. Zhang, "Macroscopic invisibility cloaking of visible light." *Nat. Commun.*, vol. 2, p. 176, 2011, https://doi.org/10.1038/ncomms1176.

[23] F. Zolla, S. Guenneau, A. Nicolet, and J. B. Pendry, "Electromagnetic analysis of cylindrical invisibility cloaks and the mirage effect." *Opt. Lett.*, vol. 32, pp. 1069–1071, 2007, https://doi.org/10.1364/ol.32.001069.

[24] X. Li, L. Chen, Y. Li, et al., "Multicolor 3D meta-holography by broadband plasmonic modulation." *Sci. Adv.*, vol. 2, 2016, Art no. e1601102, https://doi.org/10.1126/sciadv.1601102.

[25] L. Huang, X. Chen, H. Mühlenbernd, et al., "Three-dimensional optical holography using a plasmonic metasurface." *Nat. Commun.*, vol. 4. p. 2808, 2013, https://doi.org/10.1364/dh.2017.w4a.6.

[26] F. Zhang, M. Pu, P. Gao, et al., "Simultaneous full-color printing and holography enabled by centimeter-scale plasmonic metasurfaces." *Adv. Sci.*, 2020, https://doi.org/10.1002/advs.201903156.

[27] Y. Bao, Y. Yu, H. Xu, et al., "Full-colour nanoprint-hologram synchronous metasurface with arbitrary hue-saturation-brightness control." *Light Sci. Appl.*, vol. 8, p. 95, 2019, https://doi.org/10.1038/s41377-019-0206-2.

[28] S. Wang, P. C. Wu, V. C. Su, et al., "A broadband achromatic metalens in the visible." *Nat. Nanotech.*, vol. 13, pp. 227–232, 2018, https://doi.org/10.1038/s41565-017-0052-4.

[29] W. T. Chen, A. Y. Zhu, V. Sanjeev, et al., "A broadband achromatic metalens for focusing and imaging in the visible." *Nat. Nanotech.*, vol. 13, pp. 220–226, 2018, https://doi.org/10.1038/s41565-017-0034-6.

[30] X. Ma, M. Pu, X. Li, Y. Guo, and X. Luo, "All-metallic wide-angle metasurfaces for multifunctional polarization manipulation." *Opto.-Electron. Adv.*, vol. 2, p. 180023, 2019, https://doi.org/10.29026/oea.2019.180023.

[31] A. Nemati, Q. Wang, M. Hong, and J. Teng, "Tunable and reconfigurable metasurfaces and metadevices." *Opto.-Electron. Adv.*, vol. 1, p. 180009, 2018, https://doi.org/10.29026/oea.2018.180009.

[32] Q. Fan, D. Wang, P. Huo, Z. Zhang, Y. Liang, and T. Xu, "Autofocusing airy beams generated by all-dielectric metasurface for visible light." *Opt. Express*, vol. 25, pp. 9285–9294, 2017, https://doi.org/10.1364/oe.25.009285.

[33] H. Li, W. Hao, X. Yin, S. Chen, and L. Chen, "Broadband generation of airy beams with hyperbolic metamaterials." *Adv. Opt. Mater.*, vol. 7, p. 1900493, 2019, https://doi.org/10.1002/adom.201900493.

[34] W. Hao, M. Deng, S. Chen, and L. Chen, "High-efficiency generation of airy beams with huygens' metasurface." *Phys. Rev. Appl.*, vol. 11, 2019, Art no. 054012, https://doi.org/10.1103/physrevapplied.11.054012.

[35] A. E. Minovich, A. E. Klein, D. N. Neshev, T. Pertsch, Y. S. Kivshar, and D. N. Christodoulides, "Airy plasmons: non-diffracting optical surface waves." *Las. Photo.n Rev.*, vol. 8, pp. 221–232, 2014, https://doi.org/10.1002/lpor.201300055.

[36] L. Li, T. Li, S. M. Wang, C. Zhang, and S. N. Zhu, "Plasmonic airy beam generated by in-plane diffraction." *Phys. Rev. Lett.*, vol. 107, p. 126804, 2011, https://doi.org/10.1103/physrevlett.107.126804.

[37] A. Minovich, A. E. Klein, N. Janunts, T. Pertsch, D. N. Neshev, and Y. S. Kivshar, "Generation and near-field imaging of Airy surface plasmons." *Phys. Rev. Lett.*, vol. 107, p. 116802, 2011, https://doi.org/10.1103/physrevlett.107.116802.

[38] P. Lalanne, S. Astilean, P. Chavel, E. Cambril, and H. Launois, "Design and fabrication of blazed binary diffractive elements with sampling periods smaller than the structural cutoff." *J. Opt. Soc. Am. A*, vol. 16, pp. 1143–1156, 1999, https://doi.org/10.1364/josaa.16.001143.

[39] P. Lalanne and P. Chavel, "Metalenses at visible wavelengths: Past, present, perspectives." *Las Photon. Rev.*, vol. 11, p. 1600295, 2017, https://doi.org/10.1002/lpor.201600295.
[40] M. Pu, X. Li, X. Ma, et al., "Catenary optics for achromatic generation of perfect optical angular momentum." *Sci. Adv.*, vol. 1, 2015, Art no. e1500396, https://doi.org/10.1126/sciadv.1500396.
[41] M. Pu, Y. Guo, X. Li, X. Ma, and X. Luo, "Revisitation of extraordinary young's interference: From catenary optical fields to spin–orbit interaction in metasurfaces." *ACS Photon.*, vol. 5, pp. 3198–3204, 2018, https://doi.org/10.1021/acsphotonics.8b00437.
[42] D. Wang, Y. Hwang, Y. Dai, et al., "Broadband high-efficiency chiral splitters and holograms from dielectric nanoarc metasurfaces." *Small*, vol. 15, p. 1900483, 2019, https://doi.org/10.1002/smll.201900483.
[43] Y. Guo, Y. Huang, X. Li, et al., "Polarization-controlled broadband accelerating beams generation by single catenary-shaped metasurface." *Adv. Opt. Mater.*, vol. 7, p. 1900503, 2019, https://doi.org/10.1002/adom.201900503.
[44] M. R. Akram, G. Ding, K. Chen, Y. Feng, and W. Zhu, "Ultrathin single layer metasurfaces with ultra-wideband operation for both transmission and reflection." *Adv. Mater.*, p. 1907308, 2020, https://doi.org/10.1002/adma.201907308.

Supplementary Material: The online version of this article offers supplementary material (https://doi.org/10.1515/nanoph-2020-0057).